International Journal of Engineering

Journal Homepage: www.ije.ir

A Comparative Analysis of Axial and Radial Forces in Windings of Amorphous Core Transformers

B. D. Thanh*[a], T. H. Le[a], V. D. Quoc[b]

[a] *Faculty of Engineering and Technology, Quy Nhon University, Quy Nhon, Viet Nam*
[b] *School of Electrical and Electronic Engineering, Hanoi University of Science and Technology, Viet Nam*

P A P E R I N F O

Paper history:
Received 22 August 2023
Received in revised form 18 September 2023
Accepted 19 September 2023

Keywords:
Amorphous Core Transformer
Short-circuit Current
Electromagnetic Force
Radial and Axial Forces
Leakage Flux

A B S T R A C T

The aim of this study is to examine and analyze the axial and radial forces, electromagnetic forces (EMFs) acting on the low and high-voltage windings of an amorphous core transformer via the two different approaches: an analytic approach and a 3-D finite element method (FEM). Firstly, the analytic method is proposed to analyze the distribution of leakage magnetic field in the magnetic circuit and the forces acting on the transformer windings. The FEM embedded in the Ansys Maxwell tool is then proposed to compute and simulate the axial and radial forces under three different operating conditions: no-load, rated full-load, and short-circuit. The obtained results from two different methods such as the rated voltage, rated current, short-circuit current, axial and radial forces and EMFs in the low and high-voltage windings are finally compared to illustrate an agreement of methods. The validation of the methods is applied on a three-phase amorphous core transformer of 1600kVA-22/0.4kV.

***doi**: 10.5829/ije.2024.37.01a.18*

1. INTRODUCTION

The utilization of amorphous material in the magnetic circuits of distribution transformers has gained prominence since its development in 1970s. These transformers, known as amorphous transformers (ATs), have become prevalent in power systems due to their lower no-load losses compared to traditional transformers. This reduction in losses contributes to an overall decrease in the total losses of power systems. The extensive research has demonstrated that the ATs can achieve a significant reduction of 50-70% in no-load losses compared to transformers with silicon steel cores (1-5). Due to the special structure of the steel core and the coil with the rectangular shape of the ATs, the distribution of electric field and forces on the windings will be different on the same turn of the coil. Under the normal operating conditions, the electromagnetic forces (EMFs) acting on the windings are small due to the relatively small magnitude of the leakage flux. However, under the short-circuit condition, the electromagnetic forces (EMFs) generated as a result of the interaction between the leakage flux and the short-circuit current are very large, this can lead to translation, destruction, or even explosion of the windings (6-10).

In practices, among various types of transformer faults, winding faults account for approximately 33% of the total occurrences. These faults typically arise from short-circuits between turns within the high voltage (HV) or low voltage (LV) windings, between different layers of windings, between HV and LV windings, or even between phases within the same winding. In such cases, the resulting EMFs or mechanical forces (MFs) can cause bending or destruction of the transformer windings (11-16). The EMF can be further categorized into two distinct components: axial force (Fx) and radial force (Fy). The Fx generated by the interaction between the current in the winding and the axial magnetic field (By) is perpendicular to the winding axis. On the other hand, the Fy produced from the interaction between the current in the winding and the horizontal magnetic field (Bx), is parallel to the winding axis (17-22).

*Corresponding Author Email: doanthanhbao@qnu.edu.vn (B. D. Thanh)

Please cite this article as: Thanh BD, Le TH, Quoc VD. A Comparative Analysis of Axial and Radial Forces in Windings of Amorphous Core Transformers. International Journal of Engineering, Transactions A: Basics, 2024;37(01):201-212.

Wang et al. (7) provided a detailed description of the design and operation of a three-phase AT with a capacity of 630 kVA-10.5/0.4 kV. The study focused on acquiring the fundamental characteristics of the AT through standard short-circuit and no-load tests. The utilization of amorphous alloy as the iron core material in the AT offers several advantages, including reduced losses and excellent magnetization characteristics. Consequently, amorphous alloys have found widespread application in small-capacity distribution power transformers.

Zhong et al. (8) used a finite element method (FEM) to compute the stress and strain of the end covers and the winding clamps of the AT of 800 kVA/10 kV. Based on that, the shell-form transformer demonstrated the superior capability to withstand short-circuits, and historical evidence has primarily relied on the use of silicon steel iron core materials. Kumbhar and Kulkarni (23) analyzed the EMFs acting on the windings of split-winding transformers by using a nonlinear-transient field-circuit coupled finite element model. In this study, a three-phase split-winding transformer of 70MVA-220/3.6/6.9kV was simulated and examined via the FEM under both preset and postset short-circuit test conditions. Mouhamad et al. (24) conducted the short-circuit withstand tests of Metglas 2605SA1-based amorphous transformers, rated 240 to 630kVA. In this paper, the authors focused on calculating the short-circuit current and the electrodynamic forces experienced by the transformer windings. However, their work did not explicitly address the distribution of the leakage magnetic field or the axial and radial forces within the transformers. Bal et al. (25) used the FEM embedded in ANSYS Maxwell simulation program to analyze the electromagnetic transients and compute the losses, voltages, currents and magnetic fluxes of a three-phase oil-type distribution transformer with a capacity of 25kVA. Li et al. (26) presented the distribution of EMF in a three-phase power transformer of a 50MVA/110 kV under short-circuit conditions via the FEM. Jin et al. (27) explored the stress distribution characteristics of a composite wire-paper winding structure when subjected to radial electromagnetic forces. A copper-paper layered ring was employed as the experimental setup. The study involved calculating both the hoop stress distribution and the radial stress distribution within the winding structure. The FEM was then used to verify the obtained results. Zhai et al. (28) established a three-dimensional model of the transformer to investigate the electrodynamic force and deformation of transformer windings under short-circuit conditions. The distribution transformers have received limited attention in previous studies, with few investigations conducted on this specific type of transformer. Furthermore, the existing literature lacks a comprehensive model for calculating Fx and Fy in distribution transformers. However, in literature review (29-32), the FEM is employed to analyze and compute various parameters such as leakage magnetic field, leakage reactance, and electromagnetic forces in both the HV and LV windings of the transformer during short-circuit tests. In these studies, a mathematical model was proposed to calculate the current and transient electromagnetic force. The leakage magnetic field density and average electromagnetic force were provided based on FEM simulation results. These obtained results using FEM are then compared with those of the analytic method.

The EMFs can be calculated by using different methods. The analytic method can provide a comprehensive and faster solution. Unfortunately, these methods may not be applied in models with nonlinear materials, complex geometric structures, and/or boundary conditions. Therefore, the FEM method based on Ansys Maxwell 3D software in the time domain is applied to solve the problem with complex shapes, multi-physics environment, and the EMFs calculation in each part or each position of the windings. Thanh et al. (33) used 2D FEM to analyze and calculate the magnetic field for a 160kVA indefinite shape MBA. In this paper, the model is considered in a short-circuit mode with maximum current, without considering the 3D model under various operating conditions such as no-load, rated load, and three-phase short-circuit conditions on the low-voltage side.

In general, as mentioned above, the FEM to analyze and calculate the distribution of magnetic fields, fringing and leakage impedances and electromagnetic forces acting on the HV and LV windings of the MBA in short-circuit conditions. They also provided formulas to calculate the overcurrent and electromagnetic force during short-circuit conditions. The results obtained include 2D FEM images of the magnetic field density and average electromagnetic forces, which are then compared with classical analytical methods. Furthermore, there are very few research works on the magnetic field and electromagnetic force of the armorphous steel-core MBA. No research has comprehensively analyzed and evaluated various operating conditions of the armorphous MBA using 3D FEM models, progressing from analytical models to full 3D FEM models. Using a 3D FEM model approaches a nearly real representation of the MBA, allowing for the analysis of multi-physics phenomena, including mechanical, electrical, and thermal effects. This approach helps accurately to determine the winding strength in various short-circuit condition, which can be challenging to achieve through analytical methods and experiments.

Based on the development from published paper by Thanh et al. (33), in this context, the magnetic vector potential. Formulations (A) is first presented to define the distribution of leakage magnetic field in the magnetic circuit and the distribution of EMFs in the transformer windings. Then, the FEM is developed based on Ansys Maxwell 3D in the time domain to simulate electromagnetic parameters of a three-phase TA of 1600kVA, 22/0.4 kV under several operating conditions, such as no-load, rated full-load and short-circuit. The obtained results from the FEM are verified and compared with the analytic model in terms of accuracy. In addition, the EMFs acting on the HV and LV windings will be also determined in the case of a three-phase short-circuit of the LV winding. This research is conducted based on the following assumptions: (1) the neglect of eddy current effects in the windings; (2) the assumption of uniform current density in the windings; (3) the consideration of a symmetric model for analysis.

2. SHORT-CIRCUIT ELECTROMAGNETIC FORCE ANALYSIS

2. 1. Short-circuit Current

The short-circuit current flowing in the windings has the potential to cause damage to the transformer windings. This transient short-circuit current comprises two different components, namely (8, 29, 34):

$$\begin{aligned} i_{SC} &= i_{hos} + i_{dos} \\ &= I_n\sqrt{2}.\sin(\omega t - \phi - \varphi_n) + I_n\sqrt{2}.\sin(\phi + \varphi_n).e^{-\frac{R_n}{X_n}\omega t} \end{aligned} \tag{1}$$

where:

- i_{hos} is the harmonic oscillation,
- i_{dos} is the damped oscillation,
- $I_n = \frac{U_{rated}}{Z_n}$ is the root mean square (SMS) of short-circuit current (A),
- $\varphi_n = \text{arctg}\frac{X_n}{R_n}$ is the phase angle (rad),
- U_{rated} is the rated voltage
- Z_n is the short-circuit impedance (Ω),
- X_n and R_n are respectively short-circuit resistance and reactance (Ω),
- t is the time (s),
- ϕ is the angle depending on the short-circuit time (rad),
- ω is the angular frequency (rad/s).

2. 2. Analytic Model for Computation of the Leakage Magnetic Fields and EMFs in Transformer Windings

Based on Maxwell's equations, the separate equation for the stationary electromagnetic field (∂/∂t = 0) in the transformer windings associated with the current density J, the Laplace-Poisson's equation for A(x,y,z) can be obtained as follows (22, 26, 28, 33):

$$\nabla^2 \mathbf{A}(x,y,z) = \begin{cases} -\mu\mathbf{J} & \text{in the windings} \\ 0 & \text{others} \end{cases} \tag{2}$$

In three-dimensional Descartes coordinates, Equation 2 can be written as:

$$\frac{\partial^2 \mathbf{A}(x,y,z)}{\partial x^2} + \frac{\partial^2 \mathbf{A}(x,y,z)}{\partial y^2} + \frac{\partial^2 \mathbf{A}(x,y,z)}{\partial z^2} = -\mu\,\mathbf{J} \tag{3}$$

where A(x,y,z) is the magnetic vector potential, μ is the relative permeability (H/m) and J is the electric current density in the windings (A/m^2).

In Figure 1, the magnetic field is perpendicular to the plane (∂A/∂z = 0). Hence, Equation 3 can be represented as:

$$\frac{\partial^2 \mathbf{A}(x,y)}{\partial x^2} + \frac{\partial^2 \mathbf{A}(x,y)}{\partial y^2} = -\mu\mathbf{J} \tag{4}$$

where the **J** can be computed via the electric current density in the HV winding ($\mathbf{J}_1$) and LV winding ($\mathbf{J}_2$), that is:

$$\mathbf{J}_1 = \frac{W_1 i_1}{a_1 b_1};\ \mathbf{J}_2 = \frac{W_2 i_2}{a_2 b_2} \tag{5}$$

where a_1b_1 and a_2b_2 are the cross-sections of the HV and LV windings, respectively. The quantities i_1 and i_2 are the electric currents in HV and LV windings, respectively.

The magnetic vector potential **A** (x,y) in Equation 4 can be analysed in the form of a harmonic series:

$$\mathbf{A}(x,y) = \sum_j\sum_k A_{j,k}\cos(m_j x).\cos(n_k y) \tag{6}$$

where $A_{j,k}$ is the constant of integration calculation. The terms of m and n are the phase angles.

The components of a magnetic field in the x- and y-axis at the boundaries of the magnetic window are

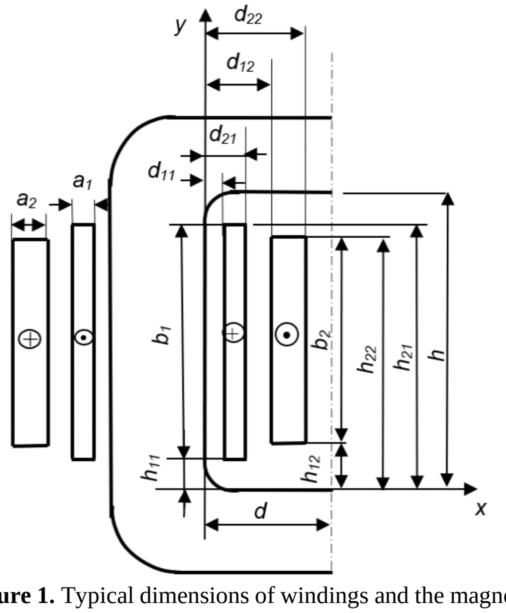

Figure 1. Typical dimensions of windings and the magnetic circuit

considered as a zero (i.e., $B_x = 0$ and $B_y = 0$). The boundary conditions (BCs) are defined as:

$$\sin(m_j d) = 0 \rightarrow m_j = (j-1)\frac{\pi}{d} \quad (7)$$

$$\sin(n_k h) = 0 \rightarrow n_k = (k-1)\frac{\pi}{h} \quad (8)$$

where j and k are the integers.
For j = k = 1 and $m_1 = n_1 = 0$, the harmonic sequence is a constant. The constant of integration $A_{j,k}$ can be generally illustrated as:

$$A_{j,k} = \frac{4\,\mu_0}{d.h}\frac{1}{m_j n_k (m_j^2 + n_k^2)} \times \begin{bmatrix} J_1\left(\sin m_j d_2^1 - \sin m_j d_1^1\right)\left(\sin n_k h_2^1 - \sin n_k h_1^1\right) \\ +J_2\left(\sin m_j d_2^2 - \sin m_j d_1^2\right) x \left(\sin n_k h_2^2 - \sin n_k h_1^2\right) \end{bmatrix} \quad (9)$$

The magnetic flux density (**B**) can be given as $\mathbf{B} = \nabla \times \mathbf{A}$, the components of **B** in the x- and y- axis at the boundaries of the magnetic window are expressed as:

$$\begin{cases} B_x = \dfrac{\partial \mathbf{A}(x,y)}{\partial y} \\ B_y = -\dfrac{\partial \mathbf{A}(x,y)}{\partial x} \end{cases} \quad (10)$$

2. 3. The Axial and Radial Forces in the Windings

As presented, the EMFs acting on the transformer windings are the interaction between the transient currents and the leakage magnetic field within the winding regions. For that, the EMF can be split into two components, i.e., the F_x and F_y as shown in Figure 2. The observed trends of these forces are as follows:

- They exert compression forces, leading to a reduction in the radius of the inner coil.
- They exert tension forces, resulting in an increase in the radius of the outer coil.
- They exert compression forces, causing a decrease in the height of both coils.

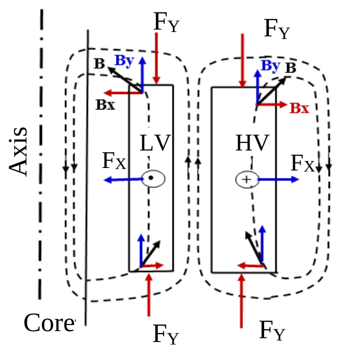

Figure 2. Components of magnetic induction field Fx and Fy in the transformer windings

⁎ *The components of EMF in the LV winding, per unit length of the winding*:
The radial force ($F_{X\text{-}LV}$) in the x-axis is defined as:

$$F_{X\_LV} = \int_{d_1^1}^{d_2^1}\int_{h_1^1}^{h_2^1} J_1 B_y\,dx\,dy = -J_1\int_{d_1^1}^{d_2^1}\int_{h_1^1}^{h_2^1}\frac{\partial \mathbf{A}(x,y)}{\partial x}dx\,dy \quad (11)$$

In the same way, the radial force ($F_{y\text{-}LV}$) in the y-axis is defined as:

$$F_{Y\_LV} = \int_{d_1^1}^{d_2^1}\int_{h_1^1}^{h_2^1} J_1 B_x\,dx\,dy = J_1\int_{d_1^1}^{d_2^1}\int_{h_1^1}^{h_2^1}\frac{\partial \mathbf{A}(x,y)}{\partial y}dx\,dy \quad (12)$$

⁎ *The components of EMF in the HV winding, per unit length of the winding*:
The radial force ($F_{X\text{-}HV}$) in the x-axis is defined as:

$$F_{X\_HV} = \int_{d_1^2}^{d_2^2}\int_{h_1^2}^{h_2^2} J_2 B_y\,dx\,dy = -J_2\int_{d_1^2}^{d_2^2}\int_{h_1^2}^{h_2^2}\frac{\partial \mathbf{A}(x,y)}{\partial x}dx\,dy \quad (13)$$

In the similar way, the radial force ($F_{y\text{-}HV}$) in the y-axis is defined as:

$$F_{Y\_HV} = \int_{d_1^2}^{d_2^2}\int_{h_1^2}^{h_2^2} J_2 B_x\,dx\,dy = -J_2\int_{d_1^2}^{d_2^2}\int_{h_1^2}^{h_2^2}\frac{\partial \mathbf{A}(x,y)}{\partial y}dx\,dy \quad (14)$$

3. ANALYTICAL TEST

The practical test problem is a three-phase amorphous core transformer of 1600kVA-22/0.4kV produced by the Sanaky transformer manufacturing factory as depicted in Figure 3. The parameters are given in Table 1. The cross-section of the core is the rectangular with the magnetic tape width b = 170 mm, thickness 2b = 340 mm; circuit window height H_{cs} = 550 mm, and distance between two cylinder centers Mo = 435 mm.

The short-circuit currents in the HV and LV windings are illustrated in Figures 4 and 5, respectively. The maximum short-circuit currents in the HV and LV windings are shown in Table 2.

Figure 3. Model of a three-phase 1600kVA-22/0.4kV

TABLE 1. Basic parameters of a three-phase amorphous core transformer

No.	Parameter	Value
1	No. of phases	3
2	Frequency [Hz]	50
3	Capacity [kVA]	1600
4	Wiring connections	Δ/Y-11
5	Hv/LV [kV]	22/0.4
6	Turns of HV/LV windings	1001/10
7	Phase current in HV/LV windings [A]	24.24/2309.4
8	Short-circuit current in HV/LV windings [A]	542.28/51664.43

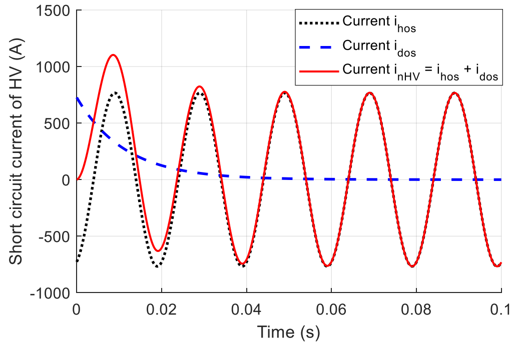

Figure 4. Distribution of the short-circuit current in the HV winding

TABLE 2. Maximum short-circuit currents in the HV and LV windings

Parameter	LV winding	HV winding
Maximum short-circuit current (A)	111090	1102.8

Based on Equation 5, the electric current densities in the LV and HV windings can be respectively calculated as:

$$J_1 = J_{nLV} = \frac{W_{LV} i_{nLVmax}}{a_1 b_1} = \frac{10 \times 111090}{23 \times 520} \times 10^6 = 92.88 \times 10^6 (A/m^2) \quad (15)$$

$$J_2 = J_{nHV} = \frac{W_{HV} i_{nHVmax}}{a_2 b_2} = \frac{1001 \times 1102,8}{37 \times 520} \times 10^6 = 57.38 \times 10^6 (A/m^2) \quad (16)$$

By using the MATLAB software, the magnetic vector potential **A** is demonstrated in Figure 6.

From Equations 11 to 14, the F_x and F_y in the LV winding are pointed out in Figures 7 and 8, respectively.

In Figure 7, it can be seen that the LV winding along the y-axis (height of winding) is pushed inwards by the F_x. The distribution of this force gradually diminishes towards the two ends of the winding. The maximum value of the radial force occurs at the middle of the winding, reaching a peak value of F_{xmax} = 24.94.10^7 N/m^2.

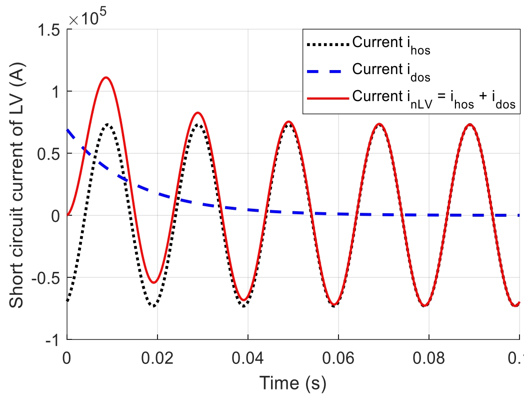

Figure 5. Distribution of the short-circuit current in the LV winding

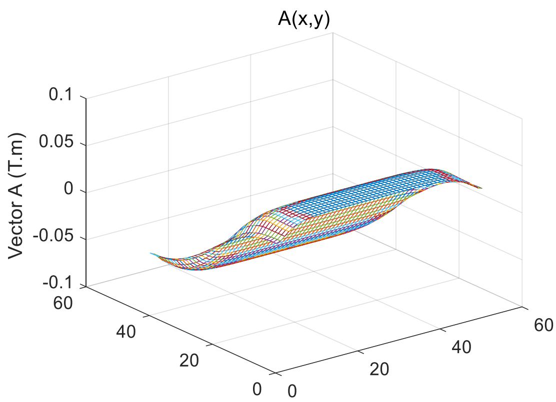

Figure 6. Distribution of magnetic vector potential

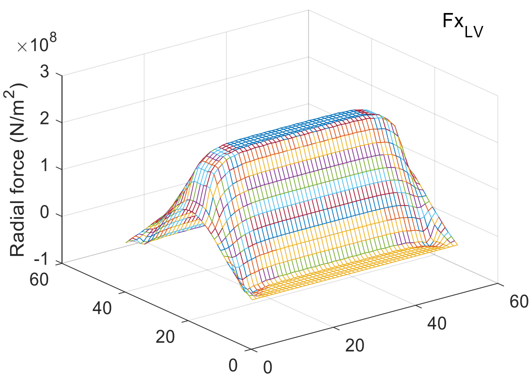

Figure 7. Radial force (F_x) in the LV winding

Figure 8 illustrates that the distribution of F_y is predominantly concentrated at the two ends of the winding, with a maximum value of F_{ymax} = ± 1.862×10^7N/m^2. In contrast, the F_y becomes zero at the midpoint of the winding.

The distribution of F_x along the y-axis (height of winding) of the HV winding is presented in Figure 9. It shows that the LV winidng is pushed far away. The distribution of this force gradually decreases to the two ends of the winding. The maximum value of radial force is at the middle of the winding with F_{xmax} = -15.44×10^7N/m^2. In the same way, the distribution of F_y is given in Figure 10. It can be seen that this force concentrates at the two ends of the winding with the maximum value of F_{ymax} = ± 3.31×10^7N/m^2. It becomes zero in the middle of the winding. The maximum EMFs acting on the HV and LV windings are represented in Table 3.

4. NUMERICAL TEST

An analytic test was given in the previous Section, in this section, the FEM is applied to verify the results from the analytic model. Keep the same prameters of the amorphous core transformer of 1600kVA – 22/0.4kV given already in Figure 1 and Table 1. The steel code of 2605HB1M has the magnetic induction field B = 1.63T. The amorphous core is pointed out in Figure 11. The geometry of the steel core generated in Ansys Maxwell 3D given in Figure 12. To minimize the calculation time, half of the cross-section in 3D is utilized due to the model inherent symmetry. In addition, the insulation material and support structure are neglected in this model (31).

The algorithm for calculation of the F_x and F_y using Ansys Maxwell 3D in different operating conditions is proposed in Figure 13.

The simulation test includes three different operating conditions: no-load, rated full-load, and short-circuit. The time intervals for each condition are as follows:

- Firstly, the no-load condition is simulated from 0 to 50 ms
- Secondly, the rated full-load condition is simulated from 50 to 100ms

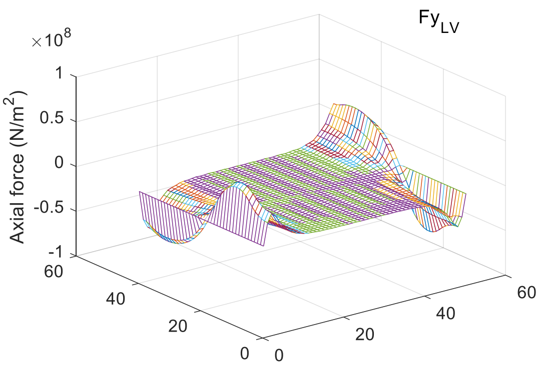

Figure 8. Axial force (F_y) in the LV winding

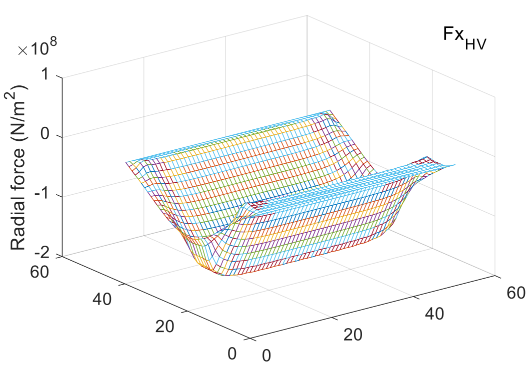

Figure 9. Radial force (F_x) in the HV winding

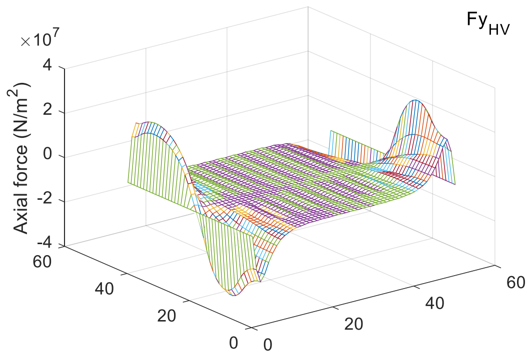

Figure 10. Axial force (F_y) in the HV winding

TABLE 3. Maximum EMFs acting on the HV and LV windings

Maximum force (10^7) (N/m^2)	LV winding	HV winding
F_{xmax}	24.94	-15.44
F_{ymax}	± 5.35	± 3.31

Figure 11. Steel core of the three-phase amorphous core transformer

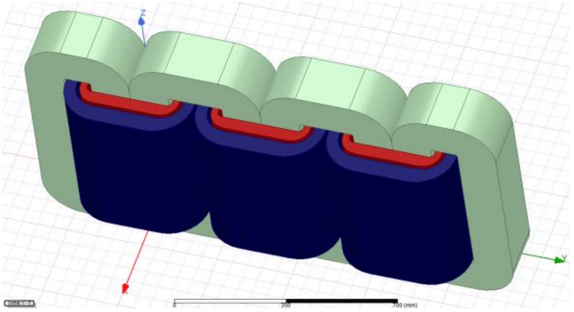

Figure 12. Geometry of the steel core generated in Ansys Maxwell 3D

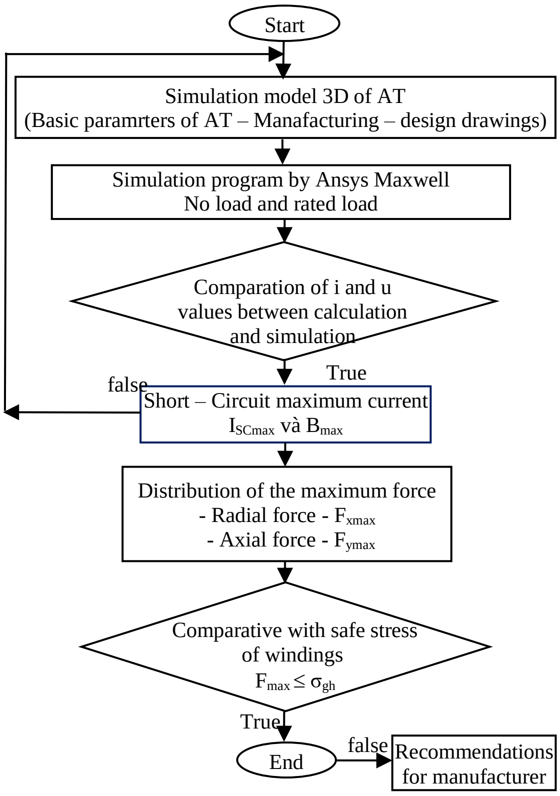

Figure 13. Algorithm for computation of Fx and Fy using Ansys Maxwell 3D

- Finally, the short-circuit condition is simulated from 150 ms to 300ms.

Figure 14 illustrates the distribution of B in the steel core of at a specific time t = 56ms.

The investigation focuses on the value and direction of the magnetic field in the magnetic circuit under both no-load and rated full-load conditions. In this analysis, the maximum magnetic flux density achieved is B_{max} = 1.78T. Subsequently, the study examines the voltages and currents in the windings of the AT, as follows.

4. 1. Under the Rated Full-load Condition The three-phase rated voltage in HV and LV windings are

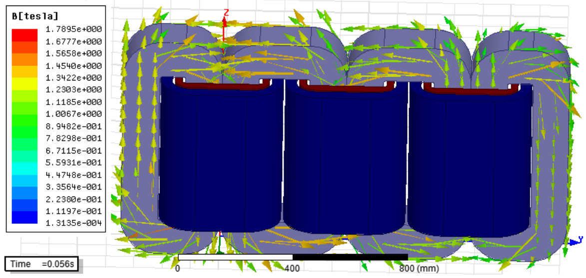

Figure 14. Distribution of magnetic flux density (B) at t = 56ms

shown in Figures 15 and 16, respectively. According to Figure 15, the simulated value of the rated voltage in the HV winding is 311320V (with a calculated value of 31112.7V. Similarly, as illustrated in Figure 16, the simulated value of the rated voltage in the LV winding is 310.7V (with a calculated value of 326.6V). The maximum error between the simulated and calculated values is 4.9%.

The three-phase rated currents in the HV and LV windings is presented in Figures 17 and 18. In Figure 17, the simulated value of the rated current in the HV winding is 33.22A (compared to a calculated value of 34.28A), whereas the simulated value of the rated current in LV winding is 3274.14A (compared to a calculated value of 3265.99A in Figure 18. The maximum error

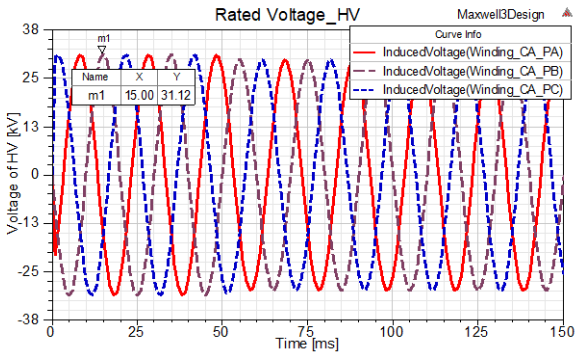

Figure 15. Three-phase rated voltage in the HV winding

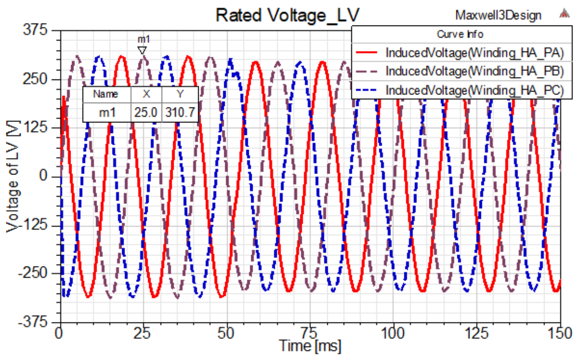

Figure 16. Three- phase fated voltages in the LV winding

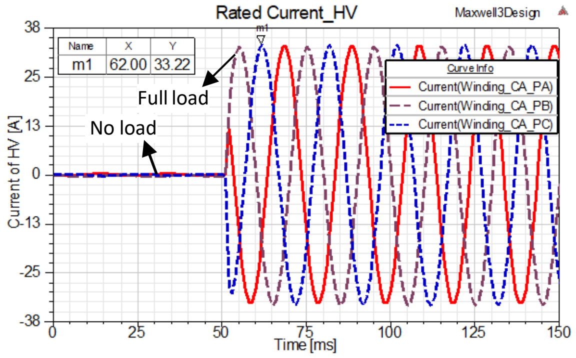

Figure 17. Three- phase rated currents in the HV winding

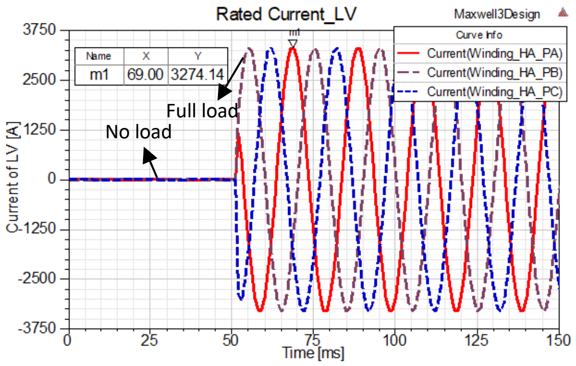

Figure 18. Three- phase rated currents in the LV winding

between the simulated and calculated values is 3.1%. The values obtained for voltages and currents using the simulation method align closely with the values derived from the analytic method under both no-load and rated full-load conditions.

4. 2. Under the Short-circuit Condition

**) Short-circuit current*

The short-circuit test of the LV winding is performed in a three-phase configuration, controlled by switch S as shown in Figure 19. The short-circuit test is initiated at t = 150ms. At this specific time, the voltage in phase B becomes zero, while the short-circuit current in phase B reaches its maximum value. The simulation is then conducted up to 300ms, with an incremental time step of Δt = 0.1ms

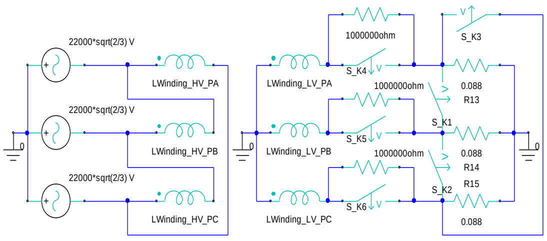

Figure 19. Diagram of control circuit

**) Distributions of leakage magnetic field and electromagnetic forces*

The problem is considered in the time domain, allowing for the analysis of the magnetic induction distribution within the magnetic circuit and windings at various operating times of the AT. Specifically, during the short-circuit period, the currents, magnetic field, and electromagnetic forces in the windings are examined at the time when the short-circuit current reaches its maximum value. Figure 20 illustrates the simulated magnetic induction at t = 159ms during the short-circuit condition.

At t = 159ms, which corresponds to the maximum short-circuit current in phase B, the leakage magnetic field within the winding intensifies to B = 2.6T, while the magnetic induction within the magnetic circuit decreases. A significant portion of the distributed leakage magnetic field is concentrated in the region between the HV and LV windings. Figures 21 and 22 showcase the short-circuit currents within the HV and LV windings, respectively.

As depicted in Figure 21, at t = 159ms, the short-circuit current in the HV winding of phase B reaches its maximum value, with I_{CA_max} = 1109.4A. This value is 33 times greater than the rated phase current. Similarly, Figure 22 demonstrates that at t = 159 ms, the short-circuit current in the LV winding of phase B attains its maximum value, with I_{HA_max} = 111076A. This value is

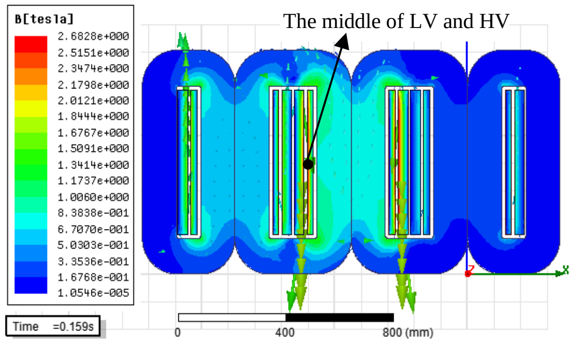

Figure 20. Magnetic induction at the time of t = 159ms

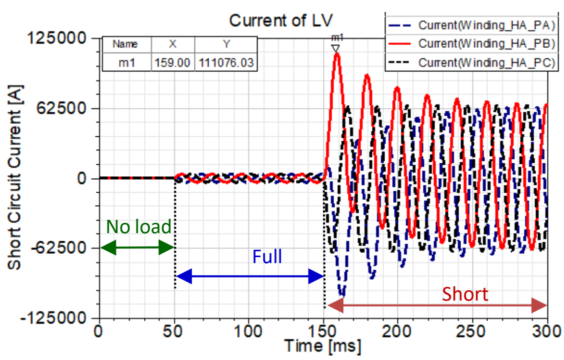

Figure 21. Short-circuit currents in the HV winding

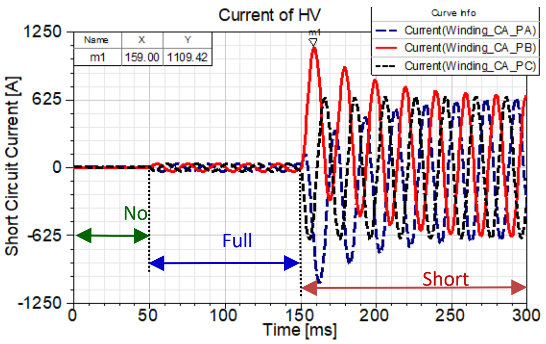

Figure 22. Short-circuit currents in the LV winding

TABLE 4. Comparion of the currents and voltages between the analytic method and FEM

Condition	Winding	Analytic method	FEM	Error %
Ratedphase voltage (V)	HV	31112.7	31120	0.02
	LV	326.6	310.7	4.9
Rated phase current (A)	HV	34.28	33.22	3.1
	LV	3265.99	3274.14	0.2
Short-circuit impulse current (A)	HV	1102.8	1109.4	0.6
	LV	111090	111076	0.01

34 times greater than the rated phase current. Table 4 presents a comparison of the currents and voltages in the HV and LV windings obtained through both the analytic method and the simulation method.

Based on the comparison results presented in Table 4, there are differences between the values obtained using the two methods. It should be noted that these disparities arise because the insulation material and support structure of the AT were disregarded in the model used for this analysis.

4. 3. EMFs Acting on the HV and LV Windings

The FEM embeded in Ansys Maxwell tool is proposed to analyze both the direction and magnitude of the magnetic field vector surrounding the winding space, as well as the maximum current density during short-circuit conditions. This enables the determination of the distributions of EMFs acting on the HV and LV windings.

At the cross-section of transformer in the Oxy plane, the EMFs can be divided into two components, i.e., $F_x = B_y. J_z$ and $F_y = B_x. J_z$.

The distributions of F_x and F_y in the LV winding at the time t = 159 ms are shown in Figure 23 and Figure 24.

As depicted in Figure 23, the F_x reaches its maximum value at the midpoint of the winding, with F_{xmax_LV} = 24.10×10^{7}N/m^2 for the LV winding. Similarly, in Figure 24, the F_y attains its maximum values at the two ends of the winding, with F_{ymax_LV} = ± 5.46×10^{7}N/m^2 for the LV winding.

Similarly, the distributions of F_x and F_y in the HV winding at the time t = 159ms are pointed out in Figures 25 and 26.

In Figure 25, the F_x gets the maximum value at the middle of the winding with F_{xmax_HV} = – 15.76×10^{7}N/m^2, whereas the F_y gets the maximum values at the two ends of the winding F_{ymax_LV} = ± 3.39×10^{7}N/m^2 in Figure 26. The maximum values of F_x and F_y and in the HV and LV windings between two methods are given in Table 5.

The maximum total F_x is concentrated at the center between the outer boundary of the LV winding and the

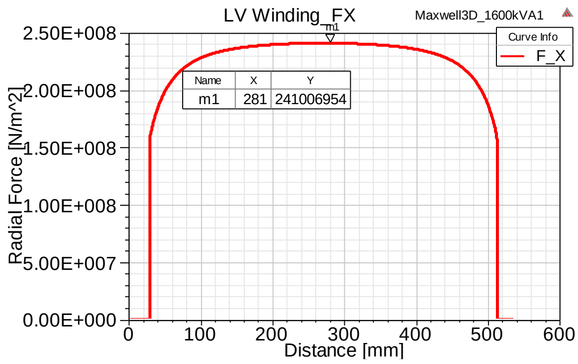

Figure 23. Distribution of F_x in the LV winding

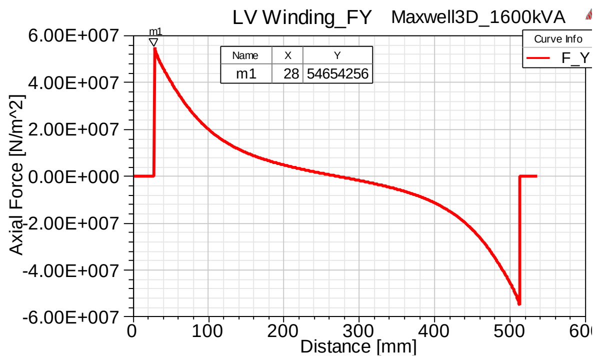

Figure 24. Distribution of F_y in the LV winding

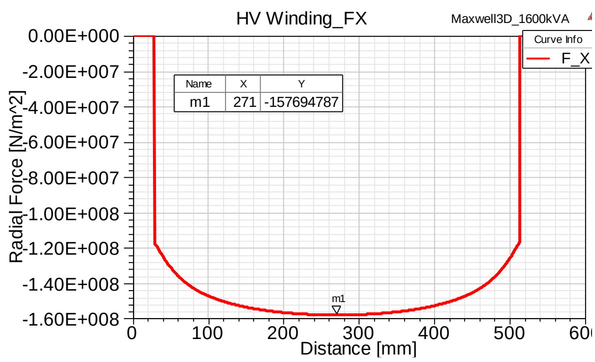

Figure 25. Distribution of F_x in the HV winding

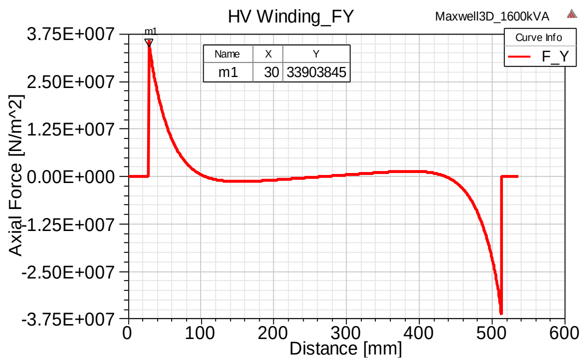

Figure 26. Distribution of the F_y in the LV winding

TABLE 5. Comparative results of the maximum values of F_x and F_y between two different methods

Winding	$F_{max}\times10^7$ (N/m^2)	Analytic method	FEM 3D	Error (%)
LV	F_{xLVmax}	24.94	24.10	3.37
	F_{yLVmax}	± 5.35	± 5.46	2.05
HV	F_{xHVmax}	– 15.44	– 15.76	2.07
	F_{yHVmax}	± 3.31	± 3.39	2.41

inner boundary of the HV winding. This force exerts a pulling effect on the winding. The maximum force, as presented in Table 5, is F_{xmax} = 24.94×10^{7}N/m^2. If the winding is considered as a solid object, the allowable stress for copper is typically within the range of $\sigma_{safe\ stress}$ = (5÷10)×10^{7}N/m^2 (15). Consequently, when a short circuit occurs with the maximum current, the maximum stress on the winding exceeds the permissible limit.

5. CONCLUSIONS

In this study, a mathematical model based on Maxwell's equations is introduced, enabling the derivation of Laplace-Poisson's equation for the magnetic vector potential formulation. Using this equation, the F_x and F_y acting on the windings of the AT of 1600kVA - 22/0.4kV have been successfully calculated. Additionally, the FEM, employing Ansys Maxwell 3D software based on Transient magnetic, is utilized to compute and simulate magnetic flux density and forces under three operating conditions: no-load, rated full-load. After that, it was confirmed that the FEM 3D simulation model was accurate, and researched the short circuit on the LV winding to find maximum the short circuit current; maximum radial and axial electromagnetic force. The obtained values of currents and voltages during rated full-load and short-circuit conditions are compared. The comparison results show that the mathematical modeling and 3D FEM completely coincide. This force may exceed the allowable limit for the winding, thereby risking its destruction, breakage, or displacement during a short circuit. Use the 3D FEM model to research and calculate and simulate the working modes of the transformer and the short circuit and destructive fault modes that experimental methods cannot do.

For future research, it is suggested to further employ the FEM based on Ansys Maxwell 3D software to investigate the distributions of EMFs at various positions in the windings. The simulation of the AT to determine the maximum force in the windings is crucial for the design, manufacturing, testing, and operation of energy-saving amorphous transformers.

6. ACKNOWLEDGEMENTS

This work was supported by the project B2022-DQN-03 sponsored by the Ministry of Education and Training, Vietnam.

7. REFERENCES

1. Steinmetz T, Cranganu-Cretu B, Smajic J, editors. Investigations of no-load and load losses in amorphous core dry-type transformers. The XIX International Conference on Electrical Machines-ICEM 2010; 2010: IEEE. 10.1109/ICELMACH.2010.5608162
2. Bahmani MA. Core loss calculation in amorphous high frequency high-power transformers with different topologies. 2011.
3. Roginskaya L, Yalalova Z, Gorbunov A, Rakhmanova J, editors. Features of amorphous steel magnetic cores for transformers operating at mains frequency. 2020 International Conference on Electrotechnical Complexes and Systems (ICOECS); 2020: IEEE. 10.1109/ICOECS50468.2020.9278451
4. Nazmunnahar M, Simizu S, Ohodnicki P, Bhattacharya S, McHenry M. Finite-element analysis modeling of high-frequency single-phase transformers enabled by metal amorphous nanocomposites and calculation of leakage inductance for different winding topologies. IEEE Transactions on Magnetics. 2019;55(7):1-11. 10.1109/TMAG.2019.2904007
5. Li D, Zhang L, Li G, Lu Z, Zhou S. Reducing the core loss of amorphous cores for distribution transformers. Progress in natural science: Materials international. 2012;22(3):244-9. https://doi.org/10.1016/j.pnsc.2012.04.005
6. Zakrzewski K, Tomczuk B, Koteras D. Amorphous modular transformers and their 3D magnetic fields calculation with FEM. COMPEL-The international journal for computation and mathematics in electrical and electronic engineering. 2009;28(3):583-92. 10.1108/03321640910950034
7. Wang Y, Zhao X, Han J, Li H, Guan Y, Bao Q, et al. Development of a 630 kVA three-phase HTS transformer with amorphous alloy cores. IEEE transactions on applied superconductivity. 2007;17(2):2051-4. 10.1109/TASC.2007.898162
8. Zhong H, Niu W, Lin T, Han D, Zhang G, editors. The analysis of short-circuit withstanding ability for a 800KVA/10KV shell-form power transformer with amorphous alloy cores. 2012 China International Conference on Electricity Distribution; 2012: IEEE. 10.1109/CICED.2012.6508689
9. Bkhaitawi A, Abdoos AA, Ebadi A. Presenting an Adaptive Restraint Method to Improve Performance of Ground Differential Protection of Power Transformer. International Journal of

Engineering, Transactions A: Basic. 2022;35(11):2213-9. 10.5829/ije.2022.35.11b.16

10. Ebadi A, Hosseini S, Abdoos A. A New Simple Method to Avoid Maloperation of Transformer Restricted Earth Fault Relay during External Fault Events. International Journal of Engineering, Transactions C: Aspects. 2021;34(9):2070-6. 10.5829/IJE.2021.34.09C.04
11. Sharifian M, Esmaeilzadeh R, Farrokhifar M, Faiz J, Ghadimi M, Ahrabian G. Computation of a single-phase shell-type transformer windings forces caused by inrush and short-circuit currents. Journal of Computer Science. 2008;4(1):51-8. 10.3844/jcssp.2008.51.58
12. Luo M, Dujic D, Allmeling J, editors. Leakage flux modelling of multi-winding transformer using permeance magnetic circuit. 2016 IEEE Applied Power Electronics Conference and Exposition (APEC); 2016: Ieee. 10.1109/APEC.2016.7468009
13. Hsieh M-F, Hsu C-H, Fu C-M, Huang Y-M. Design of transformer with high-permeability ferromagnetic core and strengthened windings for short-circuit condition. IEEE Transactions on Magnetics. 2015;51(11):1-4. 10.1109/TMAG.2015.2457956
14. Ahn H-M, Oh Y-H, Kim J-K, Song J-S, Hahn S-C. Experimental verification and finite element analysis of short-circuit electromagnetic force for dry-type transformer. IEEE Transactions on Magnetics. 2012;48(2):819-22. 10.1109/TMAG.2011.2174212
15. Dekler M. Transformer_Engineering_-_Design_and_Practice-Chapter 6: Short Circuit Stresses and Strength. no year. 2000.
16. Ahn H-M, Lee B-J, Kim C-J, Shin H-k, Hahn S-C, editors. Finite element modeling of power transformer for short-circuit electromagnetic force analysis. 2012 15th International Conference on Electrical Machines and Systems (ICEMS); 2012: IEEE.
17. Zhang H, Yang B, Xu W, Wang S, Wang G, Huangfu Y, et al. Dynamic deformation analysis of power transformer windings in short-circuit fault by FEM. IEEE Transactions on Applied Superconductivity. 2013;24(3):1-4. 10.1109/TASC.2013.2285335
18. Ahmad A, Javed I, Nazar W, Mukhtar MA. Short circuit stress analysis using FEM in power transformer on HV winding displaced vertically & horizontally. Alexandria engineering journal. 2018;57(1):147-57. 10.1016/j.aej.2016.10.006
19. Dawood K, Komurgoz G, editors. Investigating effect of Electromagnetic Force on Sandwich Winding Transformer using Finite Element Analysis. 2021 28th International Workshop on Electric Drives: Improving Reliability of Electric Drives (IWED); 2021: IEEE. 10.1109/IWED52055.2021.9376371
20. Kothavade JU, Kundu P, editors. Investigation Of Electromagnetic Forces In Converter Transformer. 2021 IEEE 2nd International Conference on Smart Technologies for Power, Energy and Control (STPEC); 2021: IEEE. 10.1109/STPEC52385.2021.9718676
21. Zhao Y, Chen W, Jin M, Wen T, Xue J, Zhang Q, et al. Short-circuit electromagnetic force distribution characteristics in transformer winding transposition structures. IEEE Transactions on Magnetics. 2020;56(12):1-8. 10.1109/TMAG.2020.3028832
22. Štafl M. Electrodynamics of electrical machines. (No Title). 1967.
23. Kumbhar GB, Kulkarni S. Analysis of short-circuit performance of split-winding transformer using coupled field-circuit approach. IEEE Transactions on power delivery. 2007;22(2):936-43. 10.1109/TPWRD.2007.893442
24. Mouhamad M, Elleau C, Mazaleyrat F, Guillaume C, Jarry B. Short-circuit withstand tests of metglas 2605SA1-based amorphous distribution transformers. IEEE transactions on magnetics. 2011;47(10):4489-92. 10.1109/TMAG.2011.2155632
25. Bal S, Demirdelen T, Tümay M, editors. Three-phase distribution transformer modeling and electromagnetic transient analysis using ANSYS Maxwell. 2019 3rd International Symposium on Multidisciplinary Studies and Innovative Technologies (ISMSIT); 2019: IEEE. 10.1109/ISMSIT.2019.8932953
26. Li Y, Xu Q, Lu Y. Electromagnetic force analysis of a power transformer under the short-circuit condition. IEEE Transactions on Applied Superconductivity. 2021;31(8):1-3. 10.1109/TASC.2021.3107799
27. Jin M, Zhao Y, Wen T, Chen W, Zhang Q, Zhu T, et al., editors. Stress Distribution Characteristics of Composite Wire-Paper Winding Structure under the Radial Electromagnetic Force. 2021 IEEE Electrical Insulation Conference (EIC); 2021: IEEE. 10.1109/EIC49891.2021.9612347
28. Zhai Y, Zhu R, Li Q, Wang X, Gu Y, Li S, editors. Simulation Research on Electrodynamic Force and Deformation of Transformer Windings under Short-circuit Condition. 2022 IEEE International Conference on High Voltage Engineering and Applications (ICHVE); 2022: IEEE. 10.1109/ICHVE53725.2022.9961358
29. Feyzi MR, Sabahi M, editors. Finite element analyses of short circuit forces in power transformers with asymmetric conditions. 2008 IEEE international symposium on industrial electronics; 2008: IEEE. 10.1109/ISIE.2008.4677272
30. Zhao Y, Wen T, Li Y, Ni H, Zhang Q, Chen W, editors. A FEM-based simulation of electromagnetic forces on transformer windings under short-circuit. 2018 IEEE International Power Modulator and High Voltage Conference (IPMHVC); 2018: IEEE. 10.1109/IPMHVC.2018.8936726
31. Dawood K, Komurgoz G, Isik F, editors. Computation of the Axial and Radial forces in the Windings of the Power Transformer. 2019 4th International Conference on Power Electronics and their Applications (ICPEA); 2019: IEEE. 10.1109/ICPEA1.2019.8911132
32. Jin M, Wen T, Chen W, Zhao Y, Wu J, Wu X, et al., editors. Influence of Frequency Components of Short-Circuit Electromagnetic Force on Vibration Characteristics of Power Transformer Windings. 2022 IEEE International Conference on High Voltage Engineering and Applications (ICHVE); 2022: IEEE. 10.1109/ICHVE53725.2022.9961671
33. Thanh BD, Tung DD, Le T-H. Computation of electromagnetic forces in the windings of amorphous core transformers. Archives of Electrical Engineering. 2023:521-39--39. 10.24425/aee.2023.145423
34. Yahiou A, Mellah H, Bayadi A. Inrush Current Reduction by a Point-on-wave Energization Strategy and Sequential Phase Shifting in Three-Phase Transformer. International Journal of Engineering, Transactions C: Aspects. 2022;35(12):2321-8. 10.5829/IJE.2022.35.12C.07

Persian Abstract

چکیده

هدف از این مطالعه بررسی و تجزیه و تحلیل نیروهای محوری و شعاعی، نیروهای الکترومغناطیسی (EMF) است که بر روی سیم‌پیچ‌های ولتاژ پایین و ولتاژ بالا یک ترانسفورماتور هسته آمورف از طریق دو رویکرد مختلف: یک رویکرد تحلیلی و یک روش محدود سه بعدی تأثیر می‌گذارند. روش عنصر (FEM). در مرحله اول، روش تحلیلی برای تجزیه و تحلیل توزیع میدان مغناطیسی نشتی در مدار مغناطیسی و نیروهای وارد بر سیم پیچ ترانسفورماتور پیشنهاد شده است. سپس FEM تعبیه‌شده در ابزار Ansys Maxwell برای محاسبه و شبیه‌سازی نیروهای محوری و شعاعی تحت سه شرایط عملیاتی مختلف پیشنهاد می‌شود: بدون بار، بار کامل نامی و اتصال کوتاه. نتایج به‌دست‌آمده از دو روش مختلف مانند ولتاژ نامی، جریان نامی، جریان اتصال کوتاه، نیروهای محوری و شعاعی و EMF در سیم‌پیچ‌های ولتاژ پایین و بالا در نهایت برای نشان دادن توافق روش‌ها با یکدیگر مقایسه می‌شوند. اعتبار سنجی روش ها بر روی یک ترانسفورماتور هسته آمورف سه فاز ۱۶۰۰kVA-22/0.4kV اعمال می شود.